Computational Mechanics
https://doi.org/10.1007/s00466-018-1614-5

ORIGINAL PAPER

Powder-scale multi-physics modeling of multi-layer multi-track selective laser melting with sharp interface capturing method

Zekun Wang[1,3] · Wentao Yan[2] · Wing Kam Liu[2] · Moubin Liu[1,3]

Received: 2 October 2017 / Accepted: 28 July 2018

Abstract
As a promising powder-based additive manufacturing technology, selective laser melting (SLM) has gained great popularity in recent years. However, experimental observation of the melting and solidification process is very challenging. This hinders the study of the physical mechanisms behind a variety of phenomena in SLM such as splashing and balling effects, and further poses challenges to the quality control of the products. Powder-scale computational models can reproduce the multi-physics process of SLM. In this study, we couple the Finite Volume Method (FVM) and Discrete Element Method to model the deposition of powder particles, and use the FVM to model the melting process, both with ambient air. In particular, a cutting-edge sharp surface capturing technique (iso-Advector) is incorporated into the Volume of Fluid Model to reconstruct the interface between different phases during the melting process. Iso-Advector is then used to capture and reconstruct the interface between molten material and ambient air, which is further used as a solid boundary for spreading the next powder layer. As such, 3D geometrical data is exchanged between these two stages repeatedly to reproduce the powder spreading-melting process of SLM incorporating different scan paths on multiple powder layers. To demonstrate the effectiveness of the powder-scale multi-physics modeling framework, typical scenarios with different fabrication parameters (Ti–6Al–4V powder) are simulated and compared with experimental observations available in literature.

Keywords Additive manufacture · Selective laser melting · Interface reconstruction · Iso-Advector · Thermal multiphase flow

1 Introduction

As a typical metallic 3D-printing technique, laser additive manufacturing (LAM) is attracting more and more attention over recent decades. Selective laser melting (SLM) is a typical LAM, and can largely shorten the manufacturing circle, reduce costs and provide consumer-designed functional components [1]. SLM has already been used in various applications, such as aerospace components [2, 3], biomedical implants [4, 5] and polymers [6]. Unfortunately, the SLM technique is still not mature enough to manufacture extremely complicated, yet crucial components due to defects like poor surface finish and porosity. Additionally, it is difficult to control the mechanical properties of the products, and the residual stress can cause undesired deformation as well. Therefore, more and more researchers are focusing on numerical simulations and experiments of metallic 3D-printing to reduce or even eliminate these defects.

For example, Aboulkhair et al. [7] experimentally studied the balling phenomenon in SLM. Balling effect often occurs when the laser scanning speed is too high or the powder layer is too thick, and this increases the surface roughness. Ma et al. [8] conducted a series of experiments with different layer thicknesses to investigate the influence of the thickness on micro-hardness and tensile properties of the products. However, it is quite difficult to thoroughly reveal the inherent mechanism only with experiments due to the lack of direct observation of the melting process.

Modeling and simulation play key roles in additive manufacturing (AM) in the aspects of improving yields, shortening R&D period, predicting and correcting anomalies, and most

✉ Moubin Liu
mbliu@pku.edu.cn

1 BIC-ESAT, College of Engineering, Peking University, Beijing 100187, China

2 Department of Mechanical Engineering, Northwestern University, Evanston, IL 60201, USA

3 State Key Laboratory for Turbulence and Complex Systems, Department of Mechanics and Engineering Science, Peking University, Beijing 100871, China

Published online: 03 August 2018

importantly, reducing production costs [9, 10]. For example, Kolossov et al. [11] studied the temperature propagation in selective laser sintering (SLS) with the Finite Element Method (FEM). The simulated temperature corresponds well with experiments, while the melting process (deformation) of the metal particles is not incorporated. Qiu et al. [12] and Panwisawas et al. [13] established a melting model of SLM using the Volume of Fluid (VOF) method to track the free surfaces while incorporating Marangoni flow and many other forces that greatly affect the melting process. They used that model to study the melting process of Ti–6Al–4V (TC4) powder during SLM and compared with experimental observations. The simulations were conducted in a single track. Matthews et al. [14] experimentally studied the metal vapor flux and denudation. They established a detailed evaporation model and simulated some small-scale melting problems while splashing phenomenon was not incorporated. Khairallah et al. [15, 16] also provided good simulations of the melting process in SLM and physics of complex melt flow and formation mechanisms of pores, spatter and denudation zones were studied.

Most of the aforementioned simulations are focused on single-layer single-track problems, while recently, an integrated Discrete Element Method-Computational Fluid Dynamics (DEM-CFD) framework has been proposed to reproduce the manufacturing process from powder spreading to melting in electron beam selective melting (EBSM) [17–20], and to simulate the manufacturing processes of single/multiple-track and multiple layers to study the formation mechanisms of defects and the influence of a variety of parameters, e.g., powder layer thickness, power, scan speed, hatching distance and scanning path. The results were qualitatively compared with experiments, showing good agreement. These works were implemented through coupling two commercial softwares (EDEM for modeling powder deposition and Flow3D for modeling powder melting process). It usually requires special skill to implement customized physical models into commercial software. For example, it is not easy to consider the influence of ambient gas when modeling powder deposition with EDEM while in many situations this can be important, especially for co-axial AM [21].

In this paper, based on our previous work of modeling the manufacturing process from powder deposition to melting in ESBM with the DEM-CFD framework, we further extend the idea to model the manufacturing process from powder deposition to powder melting in SLM. Moreover, the present work has been implemented through coupling two open source codes which allow easy inclusion of more advanced numerical models (such as the sharp interface capturing method, iso-Advector). The interaction between powder particles and with ambient gas during powder deposition or transport are modeled using a fully-coupled Finite Volume Method–Discrete Element method (FVM–DEM) approach, in which the movement of the particles is simulated using the DEM while the surrounding gas is simulated using the FVM. Also the multiphase fluid flow (with metal and ambient gas) during powder melting is modeled using the FVM, and the nonlinear temperature dependences on physical parameters are considered. Furthermore, we incorporate a newly-proposed sharp interface capturing method, iso-Advector [22], into VOF. Iso-Advector is shown to be effective in capturing and reconstructing the interface between different phases, including the molten surfaces in SLM. 3D geometrical data from reconstructed molten surface are used as solid boundaries for the powder spreading simulation to generate the packing configuration of the next powder layer. As such, the real process of SLM can be comprehensively modeled, and this is a remarkable advance over previous reports in the area of SLM [14]. In our paper, a convergence study is provided. A multiple-track manufacturing processes with different layer thicknesses of Ti–6Al–4V powders and cases with higher laser power are also simulated, and the numerical results are qualitatively compared with experimental results in literature.

2 Modeling method

2.1 Governing equations for powder deposition

In this work, powder deposition is considered as a particle-air two phase flow problem while the flow of air is solved using a FVM solver and the movement of the powder is solved using a DEM solver.

The linear and angular momentum equations for powder particles are

$$m_p \frac{d\mathbf{V}_p}{dt} = -V_p \nabla p + \mathbf{F}_{drag} + m_p \mathbf{g} + \Sigma \mathbf{F}_{p-p} + \Sigma \mathbf{F}_{p-w}, \tag{1}$$

$$\mathbf{I}_p \frac{d\omega}{dt} = \Sigma \mathbf{M}_t + \mathbf{M}_r, \tag{2}$$

where m_p, $\mathbf{V}_p$, V_p and $\mathbf{I}_p$ are the mass, velocity, volume and rotational inertia of the particle. t is time, p is the ambient pressure of air, and $\mathbf{g}$ is the gravitational acceleration. $\mathbf{F}_{drag}$ is the drag force exerted on the particle by surrounding air (without pressure gradient). In this work, the Hill Koch Model [23] is employed to calculate the drag force. $\mathbf{F}_{p-p}$ is the particle–particle interaction force, and $\mathbf{F}_{p-w}$ is the particle–wall interaction forces while relevant details can be found in [24, 25]; $\boldsymbol{\omega}$ is the angular velocity of the particle, $\mathbf{M}_t$ is the moment generated by tangential forces exerted by other particles and $\mathbf{M}_r$ is the rolling friction toque [26].

The continuity and momentum equations for air are

$$\frac{\partial \alpha_2}{\partial t} + \nabla \cdot (\alpha_2 \mathbf{V}) = 0, \tag{3}$$

$$\begin{aligned}\frac{\partial}{\partial t}(\alpha_2 \rho_2 \mathbf{V}) + \nabla \cdot (\alpha_2 \rho_2 \mathbf{V} \otimes \mathbf{V}) \\ = -\alpha_2 \nabla p - \nabla \cdot (\alpha_2 \mu_2 (\nabla \mathbf{V})) - \mathbf{S}_p + \alpha_2 \rho_2 \mathbf{g}\end{aligned} \tag{4}$$

where $\mathbf{V}$ and α_2 are the velocity and volume fraction of the second phase, air. ρ_2 and μ_2 are the density and dynamic viscosity of air. $\mathbf{S}_p$ is the source term governing the momentum exchanges between air and particle as

$$\mathbf{S}_p = \frac{1}{V_{\text{Cell}I}} \sum_{\forall j \in \text{Cell}I} \frac{V_p \beta (\mathbf{V} - \mathbf{V}_p)}{1 - \alpha_2} D(\mathbf{r}_I - \mathbf{r}) \tag{5}$$

where $V_{\text{Cell}I}$ is the volume of the air cell I, β is an empirical coefficient related to the particle void fraction $1-\alpha_2$ of the FVM cell and Reynolds number [27], $\mathbf{r}$ is the position vector of the particles and $\mathbf{r}_I$ is that of air cell I, D is a distribution function that distributes the reaction forces on fluid phase at the velocity nodes in staggered Eulerian grids [27].

Through the drag force ($\mathbf{F}_{drag}$) in Eq. (1) and the source term ($\mathbf{S}_p$) in Eq. (4), the interaction of powder particles and ambient air are fully coupled. This fully-coupled FVM-DEM approach for modeling the powder deposition within ambient air is implemented step-by-step as follows:

1. Set the initial and boundary conditions for DEM and FVM solvers.
2. Solve Navier–Stokes (N–S) equation (without source term $\mathbf{S}_p$) using FVM to predict the fluid field.
3. Get DEM data such as velocities and positions of the particles at initial time step (or latest time step) from DEM solver, determine the ID of the corresponding cells, and calculate the void fraction of both particle and air phase.
4. Calculate the drag force on particles and send this information back to DEM solver for the next time step.
5. Take the sum of the calculated drag forces weighed by particle void fraction as the source term $\mathbf{S}_p$ in the N–S Equations and solve N–S Equation (with source term $\mathbf{S}_p$) using FVM to correct the fluid field obtained in Step 2.
6. Return to Step 2 and continue the simulation until reaching the final time step.

Except for aforementioned steps, there are some other points that demand our attention. Firstly, the chosen FVM cells should be at least 3 times larger than the particle diameter to ensure the accuracy of the empirical drag force model. Secondly, the time step should be small enough to prevent unphysical penetration of wall, that is, $\Delta t < \frac{L_{checking}}{U\max}$, where $L_{checking}$ is the checking distance to judge whether this particle will collide with other particles or solid walls. In this paper, $L_{checking}$ is taken as 1.5 grid size. $U_{\max}$ is the possible maximum velocity of the particle during the simulation; Thirdly, the coupling interval should be a common multiple of the time steps of FVM and DEM solver.

2.2 Governing equations in melting process

In SLM, there are many physical phenomena (e.g., surface tension, buoyancy force, Marangoni's flow, recoil pressure and others related to air-metal interactions) that can affect the melting process and the evolution of surface morphology and pores. In order to model the multiphase thermal-fluid flows, the VOF method is used in our simulations.

VOF is a popular approach to handle multiphase problems, in which normally two phases exist in the domain. Here, we define metal as the first phase and air as the second, and their volume fraction are defined as α_1 and α_2, respectively. Naturally,

$$\alpha_1 + \alpha_2 = 1. \tag{6}$$

For convenience, we will just use α to represent α_1. If $\alpha = 0$, it means that the cell is fully occupied with air. If $\alpha = 1$, the cell is fully occupied with metal, and if $0 < \alpha < 1$, the cell contains metal and air with an interface. Thus on the interface, the density ρ, heat capacity C, dynamic viscosity μ and thermal conductivity k of the mixture are weighed by volume fraction and defined as:

$$\begin{aligned}\rho &= \alpha_1 \rho_1 + \alpha_2 \rho_2, \\ C &= \alpha_1 C_1 + \alpha_2 C_2, \\ \mu &= \alpha_1 \mu_1 + \alpha_2 \mu_2, \\ k &= \alpha_1 k_1 + \alpha_2 k_2,\end{aligned} \tag{7}$$

where the subscripts denote different phases.

In our simulation, the two phases (metal and air) are assumed to be incompressible, while properties like density change with volume fraction on the two-phase interface. Thus the continuity equation is written as

$$\frac{\mathrm{d}\rho}{dt} + \rho \nabla \cdot \mathbf{U} + \nabla \rho \cdot \mathbf{U} = 0, \tag{8}$$

where $\mathbf{U}$ is the velocity of the two-phase flow.

Many factors are crucial to the evolution of pores and surface finish. Due to the lack of experimental results, recoil

pressure is not taken into consideration in the present simulation. Therefore, the Navier–Stokes equation is written as

$$\frac{\partial}{\partial t}(\rho\mathbf{U}) + \nabla\cdot(\rho\mathbf{U}\otimes\mathbf{U}) = Dc\frac{(1-\alpha_m)^2}{\alpha_m^3 + Dcs} + \nabla \times\left[\mu\left((\nabla\mathbf{U}+\mathbf{U}\nabla) - \frac{2}{3}(\nabla\cdot\mathbf{U})\right)\right] + c\kappa\nabla\alpha - \nabla p_{\_rgh} - gh\nabla\rho + |\nabla\alpha|\frac{d\kappa}{dT}(\nabla T - \mathbf{n}(\mathbf{n}\cdot\nabla T)), \quad (9)$$

where α_m is the volume fraction of molten metal, Dc is a coefficient related to permeability, and Dcs is a small value to avoid a singularity. c is the curvature, $c = -\nabla\cdot\frac{\nabla\alpha}{|\nabla\alpha|}\mathrm{sgn}(|\nabla\alpha|) = -\nabla\cdot\mathbf{n}$, $\mathbf{n}$ is the unit normal vector at the two-phase interface, and κ is the coefficient of surface tension. According to [28], it is numerically more stable to use $p_{\_rgh}$ (the dynamic pressure) when solving the Poisson's pressure equation. In this work, the simulations are performed using the open-source code, *OpenFOAM*, which also uses the dynamic pressure $p_{\_rgh}$ ($p_{\_rgh} = p - \rho hg$ and g is the magnitude of gravitational acceleration and h is the reference hight). The last term in Eq. (9) represents thermo-capillary convection, namely, Marangoni's flow, which is caused by the difference in surface tension coefficient due to the temperature gradient ∇T, where T is temperature.

For the conservation of energy, the following equation is employed [11]:

$$\frac{\partial}{\partial t}(C\rho T) + \nabla\cdot(C\rho\mathbf{U}T) - \nabla\cdot\nabla(kT) = -L\left[\frac{\partial}{\partial t}(\rho\alpha_m) + \nabla\cdot(\rho\mathbf{U}\alpha_m)\right] - |\nabla\alpha|\left[\sigma_{sb}\left(T^4 - T_{ref}^4\right) + h_c\left(T - T_{ref}\right) - S_l\right] + \Phi, \quad (10)$$

where L is the latent heat of fusion, α_m is the volume fraction of the molten metal, σ_{sb} is the Stefan-Boltzmann constant, T_{ref} is the reference temperature, and h_c is the heat transfer coefficient. Φ and S_l are the dissipation term and source term for laser energy respectively

$$\Phi = \mu(\nabla\mathbf{U} + \mathbf{U}\nabla) : \nabla\mathbf{U}, \quad (11)$$

$$S_l = \frac{2\eta P}{\pi R_l^2}\exp\left[\frac{-2\left[(x - X_l(t))^2 + (y - Y_l(t))^2\right]}{R_l^2}\right], \quad (12)$$

where P is the laser power, η is the laser absorption coefficient, $R_l$is the effective laser beam radius and $R_l^2 = R_0^2 + \left[\frac{\lambda}{\pi R_0}(z - z_f)\right]^2$ [21], in which R_0 is the laser beam radius on the focus plane, λ is the wave length of the laser and z_f is z-coordinate of the lens focus. Lastly, x, y and z are three coordinate components of the position vector $\mathbf{x}(= x\mathbf{i}+y\mathbf{j}+z\mathbf{k})$ and $X_l(t)\mathbf{i}+Y_l(t)\mathbf{j}$ composes the laser scanning path changing with time in the x–y plane.

In order to enhance the stability of the energy equation in Eq. (10), it is recommended that the radiation term $|\nabla\alpha|\sigma_{sb}(T^4 - T_{ref}^4)$ should be solved semi-implicitly.

It is noted that in most existing works for modeling SLM, thermal parameters were usually set as constants, especially when commercial software is used. It would be more physical to consider the temperature dependencies of these parameters [29]. As such, in this work, metallic heat capacity C_1 and thermal conductivity k_1 are approximated as

$$C_1 = C_{1,0} + C_{1,1}T + C_{1,2}T^2, \quad (13)$$

$$k_1 = k_{1,0} + k_{1,1}T + k_{1,2}T^2, \quad (14)$$

where $C_{1,0}$, $C_{1,0}$, $C_{1,2}$, $k_{1,0}$, $k_{1,1}$ and $k_{1,2}$ are material properties [29].

The surface tension coefficient is given as follows.

$$\kappa = \begin{cases} \frac{\kappa_l}{1+\mathrm{erf}2}\left[1 + \mathrm{erf}\left(\frac{4}{T_l - T_s}\left(T - \frac{T_l+T_s}{2}\right)\right)\right] & T \le T_l \\ \kappa_l + \frac{d\kappa}{dT}T & T > T_l \end{cases}, \quad (15)$$

where T_s is the solidus temperature, κ_l is the surface tension coefficient of the metal at liquidus temperature, and $\frac{d\kappa}{dT}$ is considered as a material constant in present study. When the temperature of the metal is below its liquidus temperature, the coefficient is approximated by a Gaussian error function *erf*; when the temperature of the metal exceeds the liquidus temperature, a linear approximation is employed.

It is known that in rheology, solid materials can be considered as fluids with extremely high viscosity. For example, the viscosity of concrete varies from 20 to 1200 Pa s [30–32], the viscosity of glacier is around 2×10^{13} Pa s [33], and the viscosity of rocks can be as large as $1\times10^{19}\sim10^{21}$ Pa s [34]. Similarly, in our work, solid particles are also considered as fluid with extremely high viscosity. The chosen viscosity should guarantee that the relaxing time of the 'solid' is much longer than the observation or simulation time. In other words, the Deborah Number is much larger than 1 [35].

In SLM, the viscosity experiences dramatic changes with temperature during the melting process. In most existing literature [12, 13], the viscosity is assumed as a constant for modeling molten metal flow while the Darcy term needs to be included in the N–S equation when modeling the solid phase of metal. According to [36], a log approximation with polynomials can better express the temperature dependence of the viscosity:

$$\ln\mu_1 = \sum_i a_i(\ln T)^i. \quad (16)$$

Unfortunately, it is difficult to determine the coefficients a_i (i is the order of polynomial) when temperature dramatically changes during the melting process. Also if temperature greatly exceeds the fitted region, e.g., the peak temperature under the laser spot, the obtained $\ln \mu_1$ can be either unreasonably high or low rather than approaching a limit, as in physics.

In this paper, the viscosity of molten metal (first phase) is approximated as

$$\ln \mu_1 = \frac{1}{2}\mathrm{erfc}\left[\frac{4}{\ln T_l - \ln T_s}\cdot\left(\ln T - \frac{\ln T_s + \ln T_l}{2}\right)\right]\cdot (\ln \mu_s - \ln \mu_l) + \ln \mu_l, \tag{17}$$

where μ_s is the viscosity of solid phase of the metal, μ_l is the viscosity of the molten liquid metal, and *erfc* is the complementary Gaussian error function and $erfc = 1 - erf$. It is seen that when T approaches the liquidus point, the first term on the RHS of Eq. (17) approaches 0, and therefore μ_1 approaches the viscosity of the molten metal μ_l. In contrast, when T approaches the solidus point, the first term on the RHS of Eq. (16) approaches 1, and therefore μ_1 approaches the viscosity of the solid phase of the metal μ_s. Therefore in present modeling, as the viscosity is calculated by a log approximation with the complementary Gaussian error function.

Generally, the volume fraction of the molten metal is approximated linearly between liquidus and solidus point [21], and this may lead to discontinuity of the derivative of volume fraction at these two points. In this paper, the fraction is approximated using a Gaussian error function,

$$\alpha_m = \frac{\alpha_1}{2}\left[1 + \mathrm{erf}\left(\frac{4}{T_l - T_s}\left(T - \frac{T_l + T_s}{2}\right)\right)\right]. \tag{18}$$

This expression is modified from linear approximation after some trivial transformations through using a Gaussian error function. It is noted that as the fraction is approximated using the Gaussian error function rather than a linear function, the transition of molten volume fraction can be smoother. This treatment is physically more reasonable and numerically more stable.

2.3 Sharp interface capturing with iso-Advector

The surface morphology of the powder bed is extremely complicated with many cavities and pores, thus a good surface capturing method can better predict the evolution of the surface structure of the molten powder bed and internal pores. Additionally, in order to perform multi-layer SLM simulation, it is important to obtain an accurate molten surface, upon which successive layers of powder particles will be deposited on. Therefore, an accurate surface capturing method is essential.

In our work, the recently-proposed iso-Advector is employed to reconstruct the interface between two phases. Iso-Advector is a VOF-based geometric surface reconstruction method capable of capturing extremely sharp interfaces and was originally proposed by Roenby et al. [22]. It uses a novel linear interpolation scheme different from PLIC [37] and a new model which computes the cell face-interface intersection evolution in structured or unstructured meshes within a time step. Two classical validation tests, Rudman–Zalesak solid rotation test and Rudman-shearing test [38, 39] are given in "Appendix B". From the two benchmark tests, it is believed that by implementing the iso-Advector method, the surface changes during metal melting process can be reproduced more accurately, making it possible to better study the evolution of pores and surface finish and to provide a more accurate boundary for the powder-laying of next layer.

3 Procedure of multi-layer multi-track SLM modeling

CFD-DEM is a popular technique to model particulate flows, in which CFD techniques such as FDM (finite difference method) [40], FVM [41], FEM [42, 43] and LBM (lattice-Boltzmann method) [44, 45] can be used to model the fluid flows while DEM is used to model the movement and interaction of solid particles [46, 47]. It should be noted that CFD and DEM can be either fully coupled or partially coupled. If CFD and DEM are fully coupled, the DEM particles also interact with surrounding fluids, except for the interaction with contacting particles. On the other hand, CFD and DEM simulations can also be conducted sequentially. A partially coupled CFD-DEM technique can be useful to simulate the whole cycle of SLM or ESBM where DEM is first used to model the powder transport or spreading process, and CFD techniques (e.g., FVM) are then used to model the melting process of metal powder. The CFD simulation of the melting and solidifying surface is important because it will be used later as the solid boundary for the powder transport or depositing on the successive layer.

It should be noted that in particle–fluid two-phase flows, the interaction of particles and fluid flow (ambient air in AM) can be important, especially when particles are small or when the speed of fluid is not very small. A fully-coupled CFD-DEM approach is usually necessary for modeling these problems. For powder bed AM, the size of the powder particles is very small (around 40 μm) and the motion of the powders is greatly subject to the drag force from the ambient air. This may cause stratified deposition of powder particles, and therefore the influence from ambient air may not be ignored. For co-axial powder feeding AM where the speed of the ambient air is considerable, a fully CFD-DEM coupled

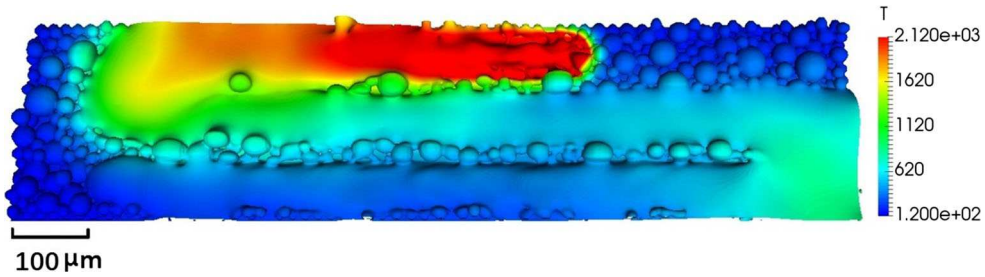

Fig. 1 Simulation of SLM in a three-track powder bed with iso-Advector capturing the molten surface. The time step is $\Delta t = 1 \times 10^{-8}$ s, the domain is 2.1 mm × 0.7 mm × 0.33 mm (the thickness of the substrate together with first layer of powder is around 0.08 mm, and the air extends to 0.33 mm) and the cell size is around 1.9 µm (approximately 15 cells in diameter). The upper boundary is set as zero-gradient for velocity, fixed value for pressure, and other patches are set as non-slip walls for simplicity. The temperature is set to be zero-gradient for all patches. Laser power is 300 W, laser radius is 42 µm, scanning speed is 1.25 m/s and the distance between tracks is 95 µm. Relevant physical parameters are listed in the "Appendix A"

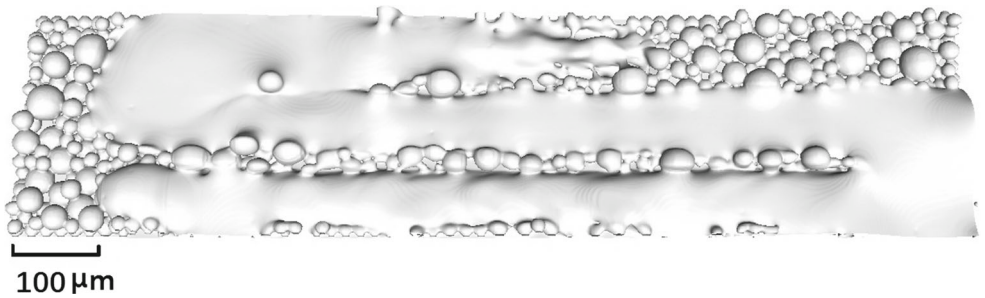

Fig. 2 The surface reconstructed by iso-Advector in *stl* form. Due to the large distance between tracks, some powder particles between tracks are not fully melted

approach is even more necessary to obtain accurate particle–fluid interaction behavior. For example, Wen et al. [21] used a fully-coupled CFD-DEM approach to model the coaxial powder flow for the laser direct deposition process.

As mentioned in Sect. 2.1, CFD and DEM are fully coupled in this work to simulate the deposition process of powder particles in SLM, with the open-source code *CFDEM* [48]. FVM is then used to model the melting process of the particles and solidifying process of the molten surface, with the open-source code *OpenFOAM* [49]. Thus, a multi-layer, multi-track modeling of SLM can be conducted, and the detailed procedure is described as follow.

(a) Deposit the powder particles for the first layer with the fully coupled unresolved FVM-DEM solver. The radii of the powders obey log-normal distribution. The motion of solid particles is calculated with the Newton's Second Law of Motion with suitable particle collision model and drag force model [50], while the motion of the surrounding gas is solved by N–S Equation (Sect. 2.1). In our simulation (from Figs. 1, 2, 3, 4), when modeling particle deposition, the same time step 2×10^{-8} s is used for both DEM and CFD simulations, and they are coupled at every time step. For DEM simulation, all the particles within the FVM cells in the Moore neighborhood of this particle's owner cell, that is, 26 surrounding cells, are found to check for collision at every time step. In DEM, the central difference scheme is used for time integration. For the continuity and momentum equations in CFD, the Euler scheme is used for time integration. It is noted that other choices of time integration algorithms are also available, while different time integration algorithms should lead to the same results, if the CFL (Courant–Friedrichs–Lewy) condition is satisfied [48].

(b) Export the coordinates and radii of the deposited particles, then use *funkySetFields* tool in *swak4Foam* (an auxiliary tool for *OpenFOAM*) to set α field on FVM cells. Set $\alpha = 1$ within the particle boundary and $\alpha = 0$ out of the particle.

(c) Use the model discussed in Sect. 2.2 to simulate melting process of the current layer with FVM (Fig. 1), where the nonlinear thermal parameters, radiation, buoyancy force, Darcy's effects and surface tension are considered. The scanning path of the laser beam is controlled by $X_l(t)\mathbf{i}+Y_l(t)\mathbf{j}$ in Eq. (12). The sharp VOF-based interface capturing method, iso-Advector, is used to track the evolution of the interface between molten metal and ambient air. In modeling the SLM process, the Euler

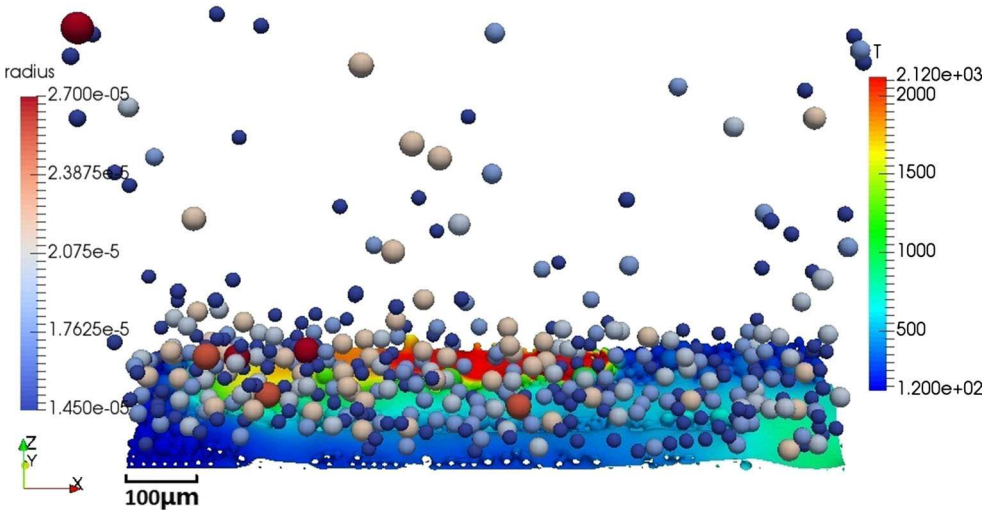

Fig. 3 Depositing powder particles for a successive layer with the fully-coupled FVM-DEM solver. The domain is 2.1 mm × 0.7 mm × 1.5 mm, and the cell size is around 250 µm, about 5 time the diameter of the powders, and $\Delta t = 2 \times 10^{-8}$ s. The *stl* wall is set as no-slip and all the other patches are set to have fixed pressure. Coefficients of restitution and friction are set as 0.3 and 0.5, Young's modulus is 120 Gpa and Poisson's ratio is 0.34. Note that this figure illustrates the generation of a reasonably packed powder bed, which may be different from the actual spreading process

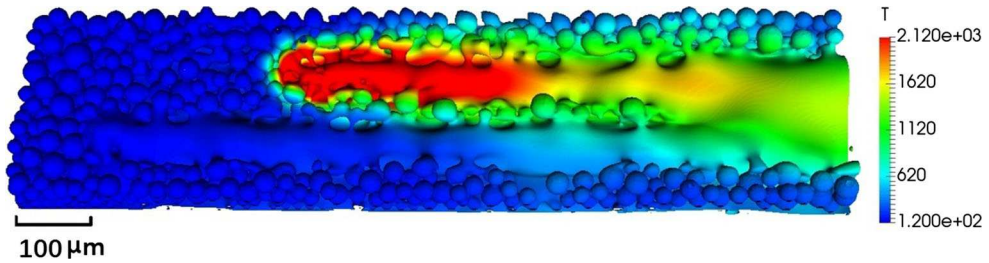

Fig. 4 Simulation of SLM on the successive layer

time scheme is used for time integration with a time step of 10^{-8} s. For spatial discretization, Gauss van Leer divergence scheme is used for the divergence containing phase transport, limited linear Gauss divergence scheme is used for face flux and linear Gauss scheme are used for gradient and Laplacian terms [49].

(d) Reconstruct the molten surface after the simulation of the first layer with iso-Advector method (Fig. 2) and use the reconstructed surface data as the solid wall boundary for FVM-DEM solver (in stl file) and deposit a successive layer of metal powders on the solidified surface (Fig. 3).

(e) Get the final coordinates and radii of the settled particles on the powder bed from the DEM solver, set α as in step *b*, and set the temperature T, viscosity μ, velocity $\mathbf{U}$, volume fraction α, pressure p and other necessary parameters from the last time step of the previous layer as the initial conditions for the successive layer.

(f) Return to Step *c* until a designated thickness of the powder bed is reached (Fig. 4).

4 Convergence study

In this section, we employ different meshes to conduct a convergence study on the two-phase single-track SLM simulation. The simulation domain of the test case is 1 mm × 0.31 mm × 0.145 mm, the laser power is 300 W and the scanning speed is 1.25 m/s.

Figure 5 shows the contours of the molten track along the scanning path on different mesh sizes. The mesh sizes for green, black, red and blue contours are 2.8, 2.4, 2.0, and 1.6 µm. As can been seen from the figure, the green and black contours are not well overlapped with the red and blue contours at the melting pool behind the laser spot. In contrast, the shapes for cases with a mesh size of 2.0 µm or 1.6 µm (blue and red) nearly overlap. Similar results are obtained for the contours in the cross-section of the track (Fig. 6). This shows that the obtained numerical results are convergent.

Another important issue in SLM is the prediction of temperature. Figure 7 shows the temperature profile along the track, from starting point to the laser spot, at the height of

Fig. 5 Contours of the molten track along the scanning path with grid sizes

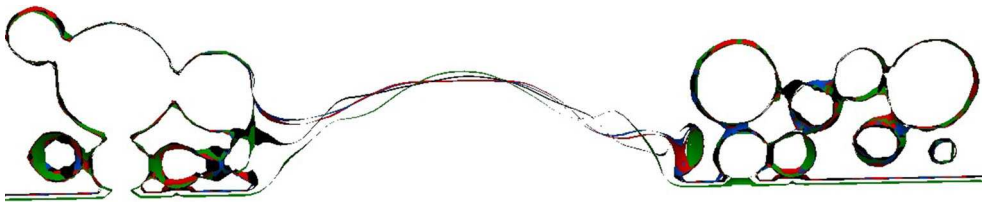

Fig. 6 Cross section contours of the molten track with different grid sizes

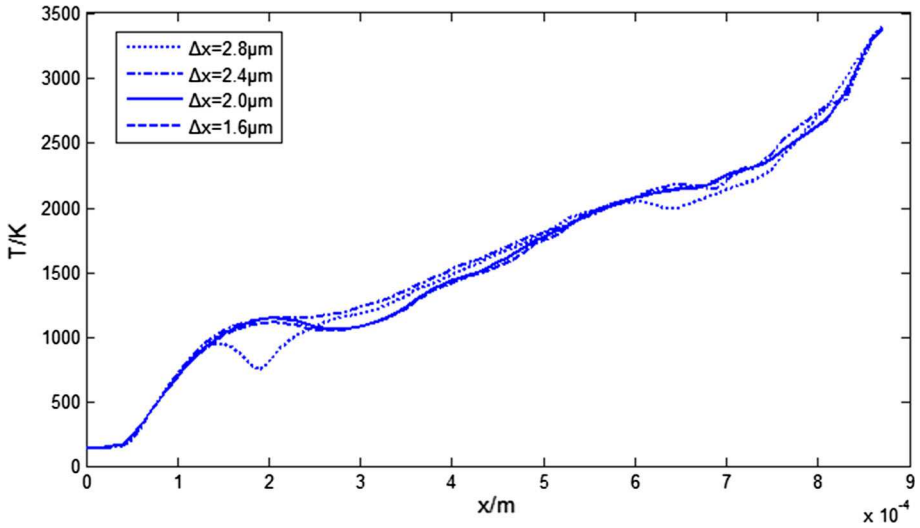

Fig. 7 Temperature profiles with grid sizes

0.0725 mm. Again, when the grid size reduces to smaller than 2.0 μm, the obtained temperature profiles basically do not change. This also shows that if the grid size is smaller than 2.0 μm, the obtained numerical results are convergent.

Additionally, the chosen time step and mesh size should satisfy the CFL condition so as to ensure that the Courant number is smaller than 1. In this convergent study (and other SLM simulations), the grid size is 1.9 μm, and the time step is 1×10^{-8} s. The total time steps for the single-track simulation above is 67,000, while all cases are run on 96 processors on Tianhe II supercomputer for 7.6 h.

5 Experimental validation

5.1 Influences of layer thickness

In order to validate the powder scale multi-physics modeling framework of multi-layer multi-track SLM with iso-Advector, we chose three typical scenarios with different solidified surface structure from Qiu's experiments [12]. In the experiments, TC4 samples were used, and related physical parameters can be found in handbooks [29]. The laser power is 400 W, scanning speed is 2.4 m/s, laser beam radius on the focus plane is 85 μm, and the thickness of powder layer in three cases are 40 μm, 60 μm and 100 μm, respectively. The discretization schemes, boundary conditions and mesh sizes are the same as those mentioned in Sect. 3. As shown in the micrographs in Fig. 8, with the increase of the layer thickness, the solidified surface becomes rougher and rougher. In Fig. 8a, though the surface is not smooth, there are no cavities or pores evolving on the surface. In Fig. 8b, some small pores with a diameter of 50–100 μm were developed. In Fig. 8c, due to large thickness and the limited laser energy, some metal powder particles were not fully molten. Additionally, since the surface tension of molten metal can be extremely high, severe balling phenomenon occurs, and the dimension of the defects is several hundred micrometers.

Figure 9 shows the simulations with corresponding layer thicknesses, 40 μm (a), 60 μm (b) and 100 μm (a). It is clearly seen that in Fig. 9a, no large pores appear on the surface of the 40-μm-thick powder bed. In Fig. 9b, there are some pores on the solidified surface, ranging from 50 to 100 μm. This also agrees with the experimental observations in Fig. 8b. If further increasing the layer thickness to 100 μm, some metal powder particles are not fully molten. Figure 9c shows that

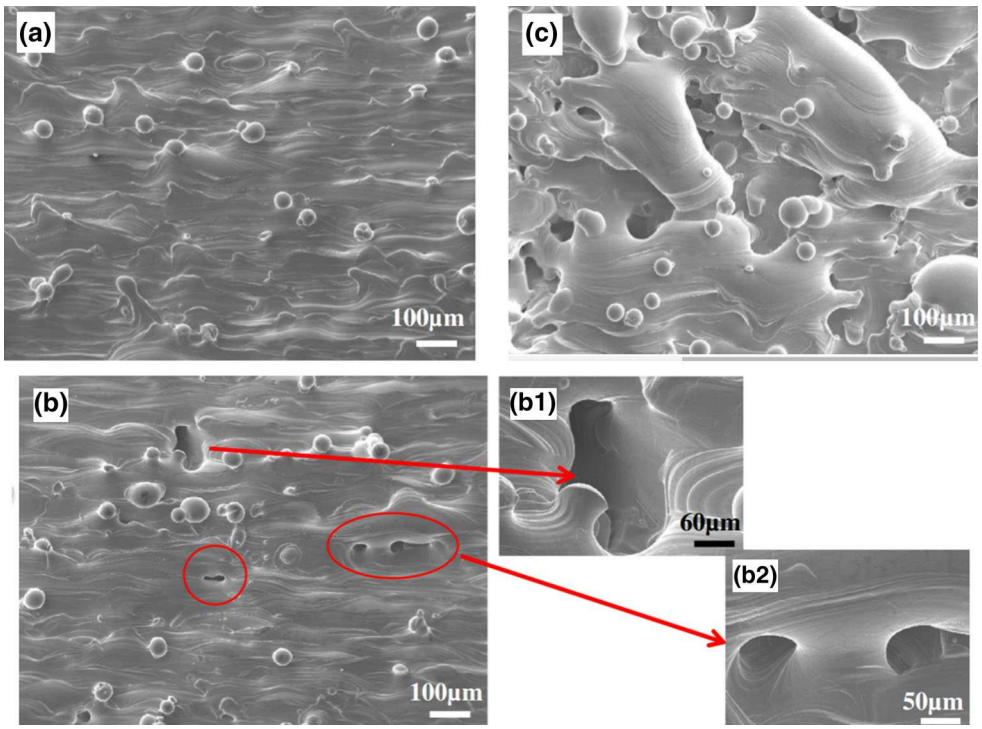

Fig. 8 Experimental results from Qiu et al. [12] with different layer thicknesses at 40 μm (**a**), 60 μm (**b**) and 100 μm (**c**)

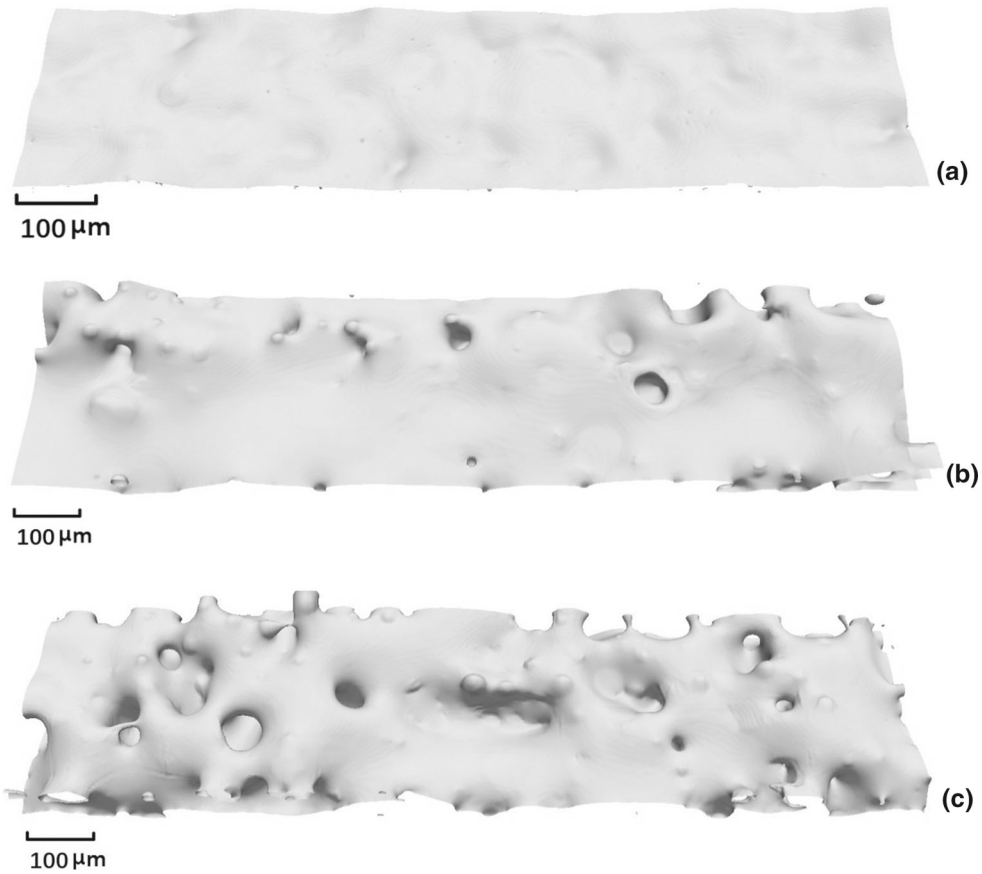

Fig. 9 Present simulations with different layer thicknesses, 40 μm (**a**), 60 μm (**b**) and 100 μm (**c**). The surface becomes rougher as the layer thickness increases

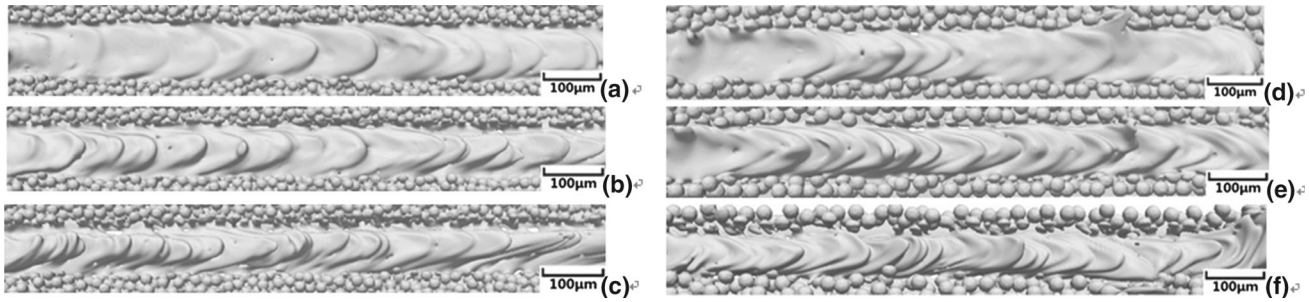

Fig. 10 Ripples occur when the laser power varies from 300 W (**a**), 600 W (**b**) to 800 W (**c**)

large some defects and the dimension of the defects is over 100 μm. This is also observed in experiments in Fig. 8c.

Overall, the simulation results from the present powder-scale multi-physics model are comparable with experimental observations. The numerical model can well reproduce the defects in different scenarios. The numerical models and computational framework can be further tested and used to study other phenomena that often occur in SLM to understand the underlying mechanism and to eliminate the defects.

5.2 Ripples on the molten track under high laser power

Another qualitative validation is the ripples caused by Marangoni force when the laser power is very intense: the large temperature gradient around the laser spot causes large gradient in surface tension, thus driving the molten metal to a certain direction (Marangoni effect). For TC4 powder, $\frac{d\kappa}{dT}$ is a negative value [29], so the Marangoni force drives the molten track flowing back towards the head of the track. The molten track solidifies very quickly for the liquid metal to flow back, accumulates and forms ripples.

In simulation, the discretization schemes, boundary conditions and mesh size are the same as those mentioned in Sect. 3. The scanning speed of the laser is 1.25 m/s, laser power are 350 W, 500 W and 600 W for the first, second and third line of figures in Fig. 10, particle diameters of first and second column of figures are 18 and 25. As you can see from Fig. 10, the ripples become more and more intense as the laser power grows due to the larger gradient of temperature and surface tension, in Fig. 10d, the ripples are even too weak to form in some area. The ripple frequency becomes higher for bigger particles, from our understanding, this is because large particle diameter causes strong instability, and the ripple period is also determined the particle diameter, but the instability caused by small particles is weak and can easily be smoothed by the strong surface tension. These phenomenon in high-power SLM was also experimentally observed by Trappa et al. [51] as shown in Fig. 11, which corresponds with our simulation very well.

Fig. 11 Experimental results by Trappa et al. [51]. Both the ripples and the piled track-heads driven by Marangoni force are well reproduced in present simulations

In conclusion, the developed computational framework can well reproduce the formation of ripples in high-power, which was experimentally observed.

6 Conclusions

This paper presents a computational framework for powder-scale multi-physics modeling of multi-layer and multi-track selective laser melting based on open source codes *CFDEM* and *OpenFOAM*. In summary, we can conclude:

1. The computational frame can reproduce the SLM processes from powder deposition to powder melting, thereby simulating multiple tracks and multiple layers. This establishes a basis to further study the influences of scanning path and successive layers.
2. The powder deposition is completed with a fully-coupled FVM-DEM solver, and thus the powder distribution can be controlled according to practical needs (size and distribution of powder particles), instead of simply generating powder particles randomly on a plane.
3. As powder melting is modeled using FVM with an advanced sharp interface capturing method, isoAdvector, and the reconstructed molten surface can be more accurate. This further leads to better solid boundary for powder spread/transport at the successive layer with more realistic powder packing.

4. Since both powder particles and ambient air are fully considered in SLM, thermal fluid flow, influences of bubbles and fusion at meso-scale can be modeled. It is shown that the simulation results of the cases with different powder layer thicknesses and laser power can actually reproduce crucial phenomena (porosity and ripples caused by Marangoni's force) in SLM quite well.

Acknowledgements Z. K. Wang and M. B. Liu acknowledge the support by the Beijing Innovation Center for Engineering Science and Advanced Technology (BIC-ESAT), and the National Key Research Project (Grant No. 2018YFB0704000). W. K. Liu acknowledges the support by the National Science Foundation (NSF) Cyber-Physical Systems (CPS) under Grant No. CPS/CMMI-1646592. W. K. Liu, and W. Yan acknowledge the support by National Institute of Standards and Technology (NIST) and Center for Hierarchical Materials Design (CHiMaD) under Grant No. 70NANB14H012. The simulations have been conducted at Tianhe II Super Computer in the National Supercomputing Center in Guangzhou with the effective support from Beijing Paratera Technology Co., Ltd.

Appendix A

Physical parameters used in the paper

Parameter	Value and units
Viscosity at melt point	$\mu_l = 0.0052$ kg/m s
Density	$\rho_1 = 4510$ kg/m^3
Heat transfer coefficient	$k_{10} = 8$ kg m/s^3 K
Heat capacity	$C_{10} = 411$ m^2/s^2 K
Preheating temperature	$T_0 = 120$ °C
Liquidus temperature	$T_l = 1659$ °C
Solidus temperature	$T_s = 1200$ °C
Latent heat	$L = 2.88 \times 10^5$ m^2/s^2
Convective heat transfer coefficient	$h = 19$ kg s^3 K
Laser radius	$R = 4.2 \times 10^{-5}$ m
Laser absorptivity	$\eta = 0.5$
Surface tension coefficient	$\kappa_1 = 1.5$ kg/s^2
Rate of change of surface tension coefficient	$\frac{\partial \kappa}{\partial T} = -0.00026$ kg/s^2 K
Viscosity of air	$\mu_2 = 1.5 \times 10^{-5}$ kg/m s
Air density	$\rho_2 = 1$ kg/m^3
Heat capacity of air	$C_2 = 1164$ m^2/s^2 K

Appendix B

In order to show the performance of this surface capturing method in extremely complicated flow, two classical validation tests, Rudman–Zalesak solid rotation test and Rudman-shearing test [38, 39], are carried out and comparisons between iso-Advector and MULES (a multi-dimensional limiter for explicit solution for interface reconstruction), are provided. Figure 12 shows the original shape of the 2D Rudman-Zalesak solid rotation test together with the shape after the rotation simulated by MULES (Fig. 12a) and iso-Advector respectively (Fig. 12b) with the same structured grid (200×200). It is obvious that the obtained shape by MULES is severely distorted, while the shape obtained by iso-Advector preserves the original shape quite well.

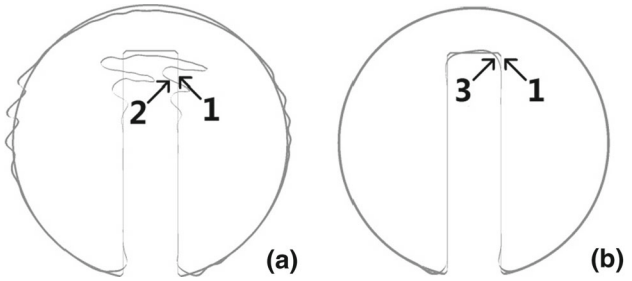

Fig. 12 Original shape of the 2D Rudman–Zalesak solid rotation test (marked as 1) together with the shape after the rotation (marked as 2 and 3 respectively) simulated by MULES (**a**) and by iso-Advector (**b**) respectively. The obtained shape by MULES deforms severely and becomes distorted. In contrast the shape obtained by iso-Advector preserves the shape quite well

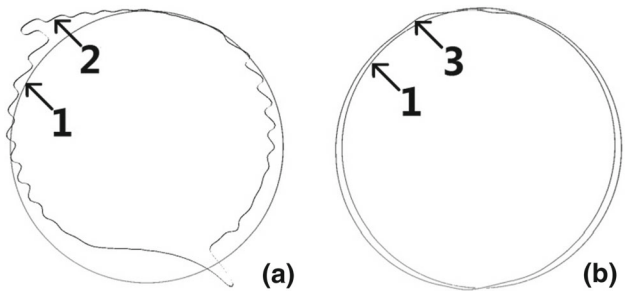

Fig. 13 Original shape (marked as 1) of the disc together with the final shape after the shearing (marked as 2 and 3 respectively) obtained by MULES (**a**) and by iso-Advector respectively (**b**). The shape obtained by MULES severely deforms and becomes zigzag

In the Rudman-shearing test, a disc is originally placed in a spiraling flow, and is sheared clockwise to form a long filament during the former half period, and then the filament is sheared anti-clockwise until the period finishes to re-form the original disk. This procedure is more complicated and can better test the performance of a surface capturing method. Figure 13 shows the original shape of the disc together with the final shape after the shearing obtained by MULES (Fig. 13a) and by iso-Advector (Fig. 13b) respectively. Again, the shape obtained by MULES severely deforms and become zigzagged. In contrast the shape obtained by iso-Advector preserves the shape much better.

References

1. Yang Y, Chen Y, Wei Y, Li Y (2016) 3D printing of shape memory polymer for functional part fabrication. Int J Adv Manuf Technol 84(9–12):2079–2095
2. Anandaraj AA (2015) Microstructure, texture and mechanical property evolution during additive manufacturing of Ti6Al4V alloy for aerospace applications. University of Manchester, Manchester
3. Hoye N, Li HJ, Cuiuri D, Paradowska AM (2014) Measurement of residual stresses in titanium aerospace components formed via additive manufacturing. Mater Sci Forum 12:5391–5396
4. Gowers SA, Curto VF, Seneci CA, Wang C, Anastasova S, Vadgama P, Yang GZ, Boutelle MG (2015) 3D printed microfluidic device with integrated biosensors for online analysis of subcutaneous human microdialysate. Anal Chem 87(15):7763
5. Murr LE, Gaytan SM, Medina F, Lopez H, Marti E (1917) Next-generation biomedical implants using additive manufacturing of complex, cellular and functional mesh arrays. Philos Trans Math Phys Eng Sci 2015(368):1999–2032
6. Laumera T, Wudyb K, Drexlerb M, Amenda P, Rotha S, Drummerb D, Schmidt M (2014) Fundamental investigation of laser beam melting of polymers for additive manufacture. J Laser Appl 26(4):042003
7. Aboulkhair NT, Everitt NM, Ashcroft I, Tuck C (2014) Reducing porosity in AlSi10Mg parts processed by selective laser melting. Add Manuf 1(4):77–86
8. Ma MM, Wang ZM, Gao M, Zeng XY (2015) Layer thickness dependence of performance in high-power selective laser melting of 1Cr18Ni9Ti stainless steel. J Mater Process Technol 215:142–150
9. Smith J, Xiong W, Yan WT, Lin S, Cheng PK, Kafka OL, Wagner GJ, Cao J, Liu WK (2016) Linking process, structure, property, and performance for metal-based additive manufacturing: computational approaches with experimental support. Comput Mech 57(5):583–610
10. Lian Y, Lin S, Yan WT, Liu WK, Wagner GJ (2018) A parallelized three-dimensional cellular automaton model for grain growth during additive manufacturing. Comput Mech 61:1–6
11. Kolossov S, Boillat E, Glardon R, Fischer P, Locher M (2004) 3D FE simulation for temperature evolution in the selective laser sintering process. Int J Mach Tool Manuf 44:117–123
12. Qiu CL, Panwisawas C, Ward M, Basoalto HC, Brooks JW, Attallah MM (2015) On the role of melt flow into the surface structure and porosity development during selective laser melting. Acta Mater 96:72–79
13. Panwisawas C, Qiu CL, Sovani Y, Brooks JW, Attallah MM, Basoalto HC (2015) On the role of thermal fluid dynamics into the evolution of porosity during selective laser melting. Scripta Mater 105:14–17
14. Matthews MJ, Guss G, Khairallah SA, Rubenchik AM, Depond PJ, King WE (2016) Denudation of metal powder layers in laser powder bed fusion processes. Acta Mater 114:33–42
15. Khairallah SA, Anderson AT, Rubenchik A, King WE (2016) Laser powder-bed fusion additive manufacturing: physics of complex melt flow and formation mechanisms of pores, spatter, and denudation zones. Acta Mater 108:36–45
16. King W, Anderson AT, Ferencz RM, Hodge NE, Kamath C, Khairallah SA (2015) Overview of modelling and simulation of metal powder bed fusion process at Lawrence Livermore National Laboratory. Mater Sci Technol 31(8):957–968
17. Yan WT, Ge WJ, Qian Y, Lin S, Zhou B, Liu WK, Lin F, Wagner GJ (2017) Multi-physics modeling of single/multiple-track defect mechanisms in electron beam selective melting. Acta Mater 134:324–333
18. Yan WT, Qian Y, Ge W, Lin S, Liu WK, Lin F, Wagner GJ (2018) Meso-scale modeling of multiple-layer fabrication process in selective electron beam melting: inter-layer/track voids formation. Mater Des 141:210–219
19. Yan WT, Smith J, Ge WJ, Lin F, Liu WK (2015) Multiscale modeling of electron beam and substrate interaction: a new heat source model. Comput Mech 56(2):265–276
20. Yan WT, Lin S, Kafka OL, Lian Y, Yu C, Liu Z, Yan J, Wolff S, Wu H, Ndip-Agbor E, Mozaffar M, Kornel E, Jian C, Wagner JG, Liu WK (2018) Data-driven multi-scale multi-physics models to derive process–structure–property relationships for additive manufacturing. Comput Mech 61:1–21
21. Wen SY, Shin YC, Murthy JY, Sojka PE (2009) Modeling of coaxial powder flow for the laser direct deposition process. Int J Heat Mass Transfer 52:25–29
22. Roenby J, Bredmose H, Jasak H (2016) A computational method for sharp interface advection. R Soc Open Sci 3:160405
23. Benyahia S, Syamlal M, O'Brien TJ (2006) Extension of Hill Koch Ladd drag correlation over all ranges of Reynolds number and solids volume fractions. Powder Technol 162:166–174
24. Renzo AD, Maio FPD (2004) Comparison of contact force models for the simulation of collisions in DEM based granular flow codes. Chem Eng Sci 59(3):525–541
25. Stevens AB, Hrenya CM (2005) Comparison of soft-sphere models to measurements of collision properties during normal impacts. Powder Technol 154(2–3):99–109
26. Zhu HP, Zhou ZY, Yang RY, Yu AB (2007) Discrete particle simulation of particulate systems: theoretical developments. Chem Eng Sci 62(13):3378–3396
27. Hill RJ, Koch DL, Ladd AJC (2001) The first effects of fluid inertia on flows in ordered and random arrays of spheres. J Fluid Mech 448:213–241
28. Macpherson GB, Nordin N, Weller HG (2010) Particle tracking in unstructured, arbitrary polyhedral meshes for use in CFD and molecular dynamics. Int J Numer Methods Bio Eng 25(3):263–273
29. Valencia JJ, Quested PN (2008) Thermophysical properties. ASM handbook, vol 15. ASM International, Materials Park, pp 468–481
30. Tattersall GH (1991) Workability and quality control of concrete. E&FN Spon, London
31. Ferraris CF, Gaidis JM (1992) Connection between the rheology of concrete and rheology of cement paste. ACI Mater J 89(4):388–393
32. Ferraris CF, Martys NS (2003) Relating fresh concrete viscosity measurements from different rheometers. J Res NIST 108(2):229–234
33. Deeley RM, Parr PH III (1972) The viscosity of glacier ice. Philos Mag 26(151):85–111
34. Renzhiglov NF, Pavlishcheva TV (1970) On the viscosity of rocks. Sov Min 6(5):582–585
35. Reiner M (2009) The Deborah number. Phys Today 17(2):62
36. Chris G (2017) 7.1 Thermophysical models, in OpenFOAM v5 user guide. OpenFOAM Foundation, London
37. Brackbill JU, Kothe D, Zemach C (1992) A continuum method for modeling surface tension. J Comput Phys 100:335–354
38. Rudman M (1998) A volume-tracking method for incompressible multifluid flows with large density variations. Int J Numer Methods Fluids 28:357–378
39. Rudman M (1997) Volume-tracking methods for interfacial flow calculations. Int J Numer Methods Fluids 24:671–691
40. Fadlun EA, Verzicco R, Orlandi P, Mohd-Yusof J (2000) Combined immersed-boundary finite-difference methods for three-dimensional complex flow simulations. J Comput Phys 161(1):35–60
41. Kim J, Kim D, Choi H (2001) An immersed-boundary finite-volume method for simulations of flow in complex geometries. J Comput Phys 171(1):132–150

42. Chang JZ, Liu HT, Su TX, Liu MB (2011) Direct numerical simulation of particle sedimentation in two-phase flow under thermal convection. Int J Comput Methods 8(4):851–861
43. Khuram W, Wang ZK, Usman K, Liu MB (2017) A multigrid finite element fictitious boundary method for fluid-solid two-phase flows. In: Liu MB et al (eds) Advances in computational engineering science. ScienTech Publisher, Mason, pp 53–70
44. Shu C, Liu N, Chew YT (2007) A novel immersed boundary velocity correction—lattice Boltzmann method and its application to simulate flow past a circular cylinder. J Comput Phys 226:1607–1622
45. Huang RZ, Wu HY (2014) An immersed boundary-thermal lattice Boltzmann method for solid–liquid phase change. J Comput Phys 227(15):305–319
46. Gan H, Chang J, Feng JJ, Hu HH (2003) Direct numerical simulation of the sedimentation of solid particles with thermal convection. J Fluid Mech 481(481):385–411
47. Fang F, Hu HH, Joseph DD (1994) Direct simulation of initial value problems for the motion of solid bodies in a Newtonian fluid. Part 1. Sedimentation. J Fluid Mech 261:95–134
48. Goniva C, Kloss C, Deen NG, Kuipers JAM, Pirker S (2012) Influence of rolling friction modelling on single spout fluidized bed simulations. Particuology 10(5):582–591
49. Jasak H (1996) Error analysis and estimation for the finite volume method with application to fluid flows. Department of Mechanical Engineering, Imperial College of London, London
50. Zhou YZ, Kuang BS, Chu KW, Yu AB (2010) Discrete particle simulation of particle-fluid flow: model formulations and their applicability. J Fluid Mech 661:482–510
51. Trappa J, Rubenchik AM, Guss G, Matthews MJ (2017) In situ absorptivity measurements of metallic powders during laser powder-bed fusion additive manufacturing. Appl Mater Today 9:341–349